Materials Today Bio 27 (2024) 101108

Contents lists available at ScienceDirect

Materials Today Bio

journal homepage: www.journals.elsevier.com/materials-today-bio

Presenting dual-functional peptides on implant surface to direct in vitro osteogenesis and in vivo osteointegration

Hui Nan [a,b,c], Yong Gou [a,b,c], Chunkai Bao [a,b,c], Hangjin Zhou [a,b,c], Haoran Qian [a,b,c], Xingjie Zan [d], Lianxin Li [e,**], Enxing Xue [a,b,c,*]

[a] Department of Orthopedics, The Second Affiliated Hospital and Yuying Children's Hospital of Wenzhou Medical University, Wenzhou, Zhejiang Province, China
[b] The Second School of Medicine, Wenzhou Medical University, Wenzhou, Zhejiang Province, China
[c] Key Laboratory of Orthopedics of Zhejiang Province, Wenzhou, Zhejiang Province, China
[d] Wenzhou Institute, University of Chinese Academy of Sciences, Wenzhou, Zhejiang, 325001, China
[e] Department of Orthopaedics Surgery, Shandong Provincial Hospital Affiliated to Shandong First Medical University, Jinan, Shandong, 250021, China

ARTICLE INFO

Keywords:
Peptide
Osteointegration
Coating
Implant
Dual functionalities

ABSTRACT

The complex biological process of osseointegration and the bio-inertness of bone implants are the major reasons for the high failure rate of long-term implants, and have also promoted the rapid development of multifunctional implant coatings in recent years. Herein, through the special design of peptides, we use layer-by-layer assembly technology to simultaneously display two peptides with different biological functions on the implant surface to address this issue. A variety of surface characterization techniques (ellipsometry, atomic force microscopy, photoelectron spectroscopy, dissipation-quartz crystal microbalance) were used to study in detail the preparation process of the dual peptide functional coating and the physical and chemical properties, such as the composition, mechanical modulus, stability, and roughness of the coating. Compared with single peptide functional coatings, dual-peptide functionalized coatings had much better performances on antioxidant, cellular adhesion in early stage, proliferation and osteogenic differentiation in long term, as well as in vivo osteogenesis and osseointegration capabilities. These findings will promote the development of multifunctional designs in bone implant coatings, as a coping strategy for the complexity of biological process during osteointegration.

1. Introduction

With the aging of the population and the increasing number of patients with bone diseases, the demand for bone implant materials is increasing[1]. Due to the biological inertness of titanium (Ti)-based bone implants currently used clinically, the long-term implant failure rate is as high as 17.9 % [2], which brings huge economic burden and psychological pressure to patients. The low bio-fusion degree between bone implants and surrounding bone tissue, called osseointegration, is an important reason for the failure of implantation [3].

Osseointegration is a complex biological process: in the early stage of implantation, extracellular matrix proteins, polysaccharides and proteoglycans are first adsorbed on the surface of the implant [4,5]. Subsequantly, osteoblasts, macrophages, and neutrophils migrate to the bone-implant interface [6]. Ideally, after a series of bone formation and conduction processes, the bone-implant interface can gradually form a tight osseointegration without direct contact and without fibrous connective tissue intervention [7]. Obviously, osseointegration is the result of the synergistic interaction between the implant and a variety of cells and the biological factors they secrete. The physical and chemical properties (wettability, roughness, surface composition, etc.) of the implant surface are crucial factors affecting osseointegration [8]. Anchoring biomolecules to the implant surface that directly participate in biological processes, is much effective in inducing bone formation [9]. It had been reported that biomolecules, such as extracellular matrix (ECM) proteins, peptides, growth factors, polysaccharides, and nucleotides, were fixed on the surface of implants to promote bone regeneration around implants [10], thereby improving bone structure and

* Corresponding author. Department of Orthopedics, The Second Affiliated Hospital and Yuying Children's Hospital of Wenzhou Medical University, Wenzhou, Zhejiang Province, China.
** Corresponding author.Department of Orthopaedics Surgery, Shandong Provincial Hospital Affiliated to Shandong First Medical University, Jinan, Shandong, 250021, China.
E-mail addresses: 13505312449@163.com (L. Li), xueenxing@wmu.edu.cn (E. Xue).

https://doi.org/10.1016/j.mtbio.2024.101108
Received 3 March 2024; Received in revised form 18 May 2024; Accepted 31 May 2024
Available online 4 June 2024

increasing the rate of implant osseointegration.

Peptides are a type of short sequence amino acid polymers with defined structures and specific biological functions [11]. In comparison to proteins, peptides possess a smaller molecular weight, are more readily synthesisable and have a reduced cost, and their structures are demonstrably more stable and easier to conserve. Furthermore, peptides can be designed to meet specific biological requirements by regulating the amino acid sequence flexibly. This allows peptides to perform a variety of biofunctions, including those related to bone formation. The utilization of peptides as a means of fabricating bioactive coatings presents a novel avenue for the fabrication of bio-functional titanium and titanium alloy implants in the realm of orthopedics [12]. For example, bone forming peptide (BFP) derived from immature bone morphology protein 7 (BMP-7), a 15 amino acid peptide (GQGFSYPYKAVFSTQ), had higher osteogenic activity than the mature BMP-7 [13]. Arginine-glycine-aspartic acid sequence (RGD), a peptide with three amino acid sequences, could promote the adhesion and proliferation of osteoblasts on orthopedic implants, thereby shortening the implantation cycle and improving the success rate of implantation [14].

A growing body of evidence demonstrated that the interface formed by dual-functional coating was more effective in meeting the complex biological demands of the osseointegration process, leading to a greater likelihood of achieving osseointegration compared to the interface formed by single-functional coating [15,16].In recent years, the strategy for constructing dual-functional peptides on the surface of bone implants has emerged as a research focus of increasing interest [17]. The strategies for fixing peptides were typically divided into two steps: firstly, the modification of the implant surface with highly active functional groups; and secondly, the chemical grafting of the fused peptide by efficient reactions, such as click chemistry or carbene chemistry, depending on the type of modified group in step one [18]. [19]. Fusing two monofunctional peptides into a single peptide and subsequently immobilizing the fused peptide on the surface of a bone implant is a straightforward and relatively simple method [20].However, the fusion peptide requires complex and sophisticated structural design to provide the single peptide with sufficient separated space to ensure its biofunction. Consequently, the sequence of the fused peptide are usually longthy, which results in a relatively expensive synthesis burden [20] Furthermore, the strategy presents difficulties in presenting the single peptide in the fused peptide in the expected orientation to achieve the desired outcomes. The strategy of fixing two single-functional peptides on the surface of bone implants is another feasible and realistic strategy. Taking advantage of coordinative interaction, the bio-adhesive molecule, tannic acid (TA) coordinately bonded with the calcium in alginate-Ca hydrogel, was used to physically adsorb E7 (EPLQLKM, with ability to improve adhesion, proliferation and migration of bone marrow stem cells (BMSCs)) and P15 (GTPGPQGIAGQRGVV, promoting bone formation) peptides [21]. The hydrogel modified with E7 and P15 promoted the recruitment of BMSCs and deposition of bone ECM, thereby enhancing the performance in rabbit osteochondral defect model. Utilizing the adhesion of poly-DOPA peptides to titanium substrates, several functional peptides fused with DOPA peptides could be jointly displayed on the surface of the implant and demonstrated good bone regeneration effects in the in vivo trial [22]. Similarly, clickable chemical groups could be displayed on the surface of the implant by poly-DOPA peptides, which was further modified with the dual functional peptides through bio-orthogonal reactions [23] Physical adsorption of functional peptides on the surface of the implant was a relatively simple method, but it was difficult to ensure the long-term stability of the deposited peptide and the osseointegration effect [24]. Chemical modification usually faced harsh chemical reaction conditions and potential toxicity of catalyst used in the following modification [25]. An efficient and straightforward method for generating robust peptides coating on implant surfaces is urgently needed.

Polyphenols contain multiple phenol groups in their molecular structure and are widely present in plants, and more than 8000 polyphenols have been identified so far [26]. Polyphenols have anti-inflammatory and antioxidant effects, which have been approved to be beneficial to bone regeneration [27]. In addition, polyphenols had strong multiple interactions with polycations which had been demonstrated to construct various assemblies, including coatings, vesicles, nanoparticles and other assemblies [28]. In a previous report, taking advantage of the interaction between hexalysine (Lys6) and tannic acid, a bifunctional peptide coating via layer-by-layer assembly was described, by linking the functional peptides with Lys6 [29]. In comparison to the techniques of chemical fixation and physical adsorption of immobilised proteins, the LBL method is characterized by its gentler approach, its simplicity and ease of handling, and its avoidance of the toxicity of chemical reagents. In addition, this strategy markedly increases the density of peptides in the coating in comparison to previous coupling of peptides to polyelectrolytes employed in LBL [30]. However, the interaction between Lys6 and tannic acid was not as robust as anticipated, resulting in a coating that was not particularly stable over time and could not support an extended period of osseointegration. It had been reported that the polyarginine exhibited more reactive to tannic acid than polylysine [31]. Inspired by this, we speculated that a polyarginine-based peptide-polyphenol coating could be constructed with enhanced stability, thereby achieving the increased osteointegration. As shown in Scheme 1A, the designed peptide was consisted with three parts, 1) in head, positively charged hexa-arginine (R6) that could form an assembly with polyphenols; 2) in tail, a peptide sequence (RGD or BFP) with specific biological functions; 3) a flexible linker in the middle, which were used to ensure the biological functions of peptides. The rationale for selecting BFP1 is not merely structural stability, which renders it resistant to denaturation, but also the absence of immunogenic issues, as well as its capacity to induce osteogenesis with angiogenesis (a crucial step in the process of osteointegration) [32]. As shown in Scheme 1B, considering the technical advantages of layer-by-layer (LBL) assembly (mild assembly conditions, wide substrate trialability, and independence from the shape of the substrate) [33], we modified the implant with polyphenol (tannic acid, TA) and dual-functional peptide (RGD and BFP) functionalized surface through the multiple interactions (hydrogen bond and electrostatic interaction) between positively charged R6 and TA. Our results demonstrated that this strategy could construct the surface of solo- or/and dual-functional peptides, which exhibited excellent osteogenic effects in vitro experiments and enhanced osseointegration capabilities in the implant of animal models (scheme 1C).

2. Materials and methods

2.1. Materials

Tannic acid (TA), hydrogen peroxide (H_2O_2, 30 % in weight), ammonia (25 % in weight), hydrochloric acid (HCl), sulfuric acid (H_2SO_4, 98 % in weight), 4,6-diamidino-2-phenylindole (DAPI), sodium hydroxide (NaOH), ethanol, tris(hydroxymethyl)-aminomethane (Tris), Triton X-100, Paraformaldehyde (4 %), and sodium β-glycerophosphate were purchased from Sigma. R6-BFP (R6-linker-GQGFSYPYKAVFSTQ, Mw 2749, 95 %), R6-RGD (R6-(linker-RGD)3, Mw 2336, 95 %), MCA-labeled R6-RGD (R6-RGD-MCA, Mw 5956, 95 %) and TAMRA-labeled R6-BFP (R6-BFP-TEMRA, Mw 6083, 95 %) were ordered from Nanjing Peptide Valley Biotechnology Co., fetal bovine serum (FBS), alizarin red S, BCIP/NBT alkaline phosphatase kit, ferric reducing antioxidant power (FRAP) kits, Dulbecco's modified Eagle's medium (DMEM), Cell Counting Kit-8 (CCK-8) and Vitamin C were purchased from Beyotime Institute of Biotechnology. Glass coverslips and silicon wafers were cleaned by piranha solution (vol:vol, 70 % concentrated sulfuric acid and 30 % hydrogen peroxide) at 90 °C for 2h, then by anhydrous ethanol and deionized water under sonication, finally dried under airflow. The sensor of gold-coated quartz crystal microbalance with dissipation was cleaned by a mixture of H_2O_2 (30 %) $NH_3{\cdot}H_2O$ (25 %), and H_2O at 75 °C for 1 h, then thoroughly rinsed by deionized wate under sonication, and

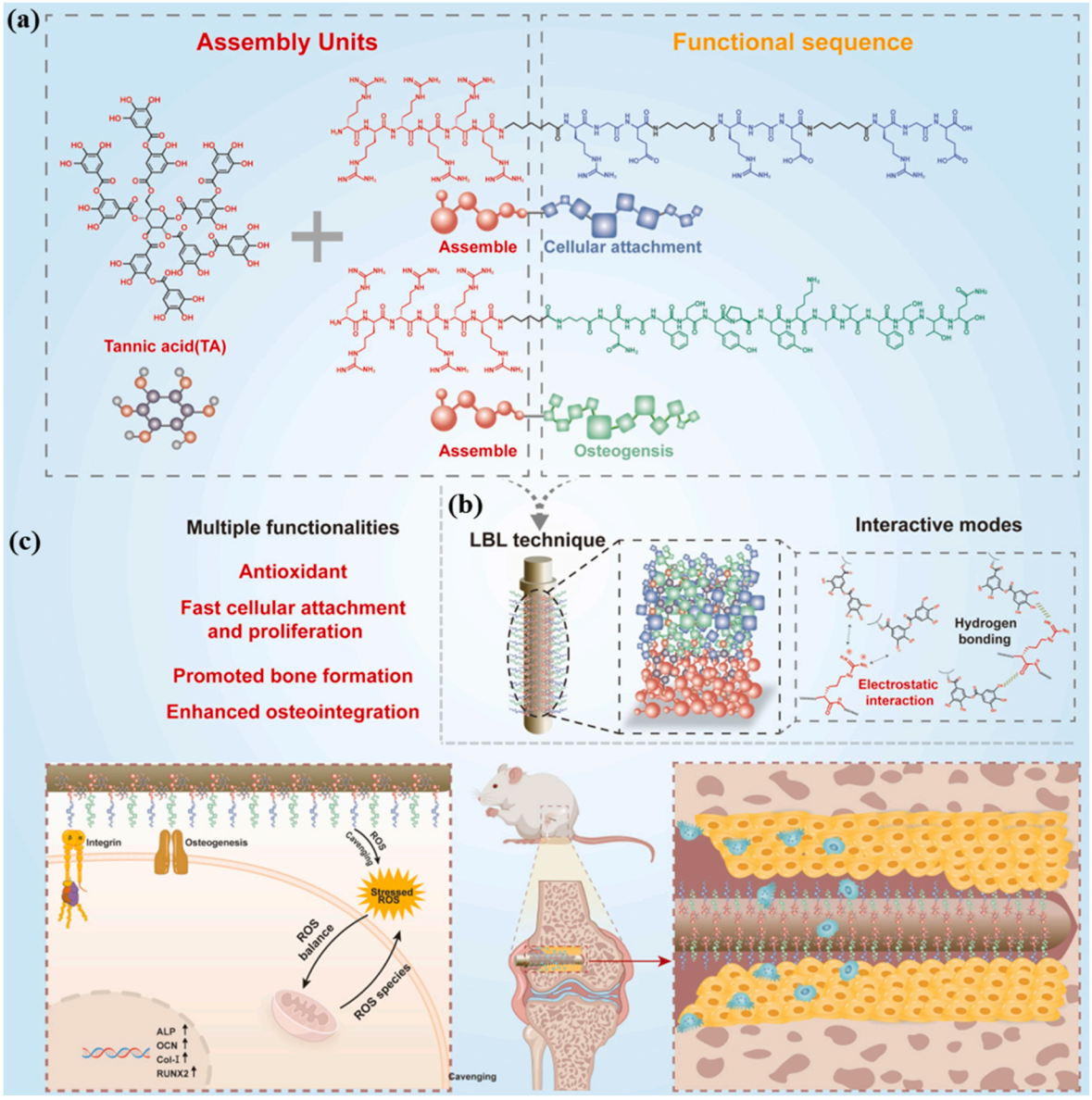

Scheme 1. Schematic illustration of the strategy for dual peptide functionalized surface. (A) the chemical formula of TA, and the designed R6-BFP and R6-RGD; (B) the LBL technique and the interactions between TA, and the peptides; (C) the biological activities of the dual peptide functionalized surface.

dried under airflow. Ti rods and Ti plates were cleaned by 75 % ethanol then the deionized water under sonication, finally dried under airflow. All water used in experiments are deionized water if not specially addressed.

2.2. Fabrication of the TA/RGD, TA/BFP, and TA/RGD&BFP films

The fabrication of TA/RGD, TA/BFP, and TA/RGD&BFP films were followed by a classic LBL technique as previously reported [34]. Briefly, the cleaned substrates (glass coverslip, silicon wafer, Ti rod and Ti plate) were immersed into the solutions of TA (1 mg/mL) and peptides (1 mg/mL, R6-BFP, R6-RGD, or the mixture of R6-BFP and R6-RGD with the fixed mass ratio 1:1 of R6-BFP and R6-RGD) alternatively for 10 min, until the desired numbers or thickness of the coating reached. The pH values of TA (1 mg/mL) and peptides at 5.5, pH 7.0, and pH 8.5 were buffered with 10 mM Tris-HCl, with adjustment of 0.1 M HCl and NaOH. Between each dipping of TA or peptide, the substrates were thoroughly washed by deionized water and dried under airflow. The prepared sample was labeled as $(TA/peptide)_{n\text{-}pH}$, in which n was the number of bilayers or the dipping cycles and the pH was the pH values of solutions during LBL.

2.3. Stability test

$(TA/peptide)_n$ films coated onto silica substrate were incubated into PBS or DMEM with/without proteinase K at pH 7.4. After soaking at setup time points (from day 1–21), the films were thoroughly washed by water and dried by nitrogen flow, and the thickness of the film was tested by ellipsometry to evaluate the stability by the percentage of remained thickness, which was calculated from the following equation: (original thickness-thickness at tested time)/original thickness.

2.4. Characterization of the TA/RGD, TA/BFP, and TA/RGD&BFP films

The deposition of TA and peptide was monitored by quartz crystal microbalance with dissipation (QCM-D) (E4, Biolin). With injection rate 50 μL/min, the change of resonance frequency (ΔF) and energy dissipation (ΔD) under different overtones ($\nu = 1, 3, 5, 7, 9 \ldots$) were recorded

in real time, and data at $\nu = 3$ were used for figuring and kinetic fitting. The deposition kinetics of peptide was exampled by investigating the deposition of peptide onto the film of $(TA/peptide)_{3.5}$. The ΔF data at $\nu = 3$ was fitted by the equation: $\Delta F = A_0 * \exp(-t/T)$, where the t is the deposition time, and A_0 and T are the constants obtained from the fitted curve and reflected the kinetic rate. The thickness in the liquid (tested by QCM-D) was obtained under the Voigt viscoelastic model [35]. The thickness in dry was measured by ellipsometer (M2000UI, J. A. Woollam Co.). The morphology, roughness and mechanical properties of the coating were tested by atomic force microscope (AFM, Dimension Icon, Bruker). After fixing the samples, which was soaked into water 5 min for stabalization, then measured in PeakForce QNM mode in fluid at randomly selected areas with a resolution of 256 × 256 pixels. A contact model is necessary for analyzing the obtained force curves, the Johnson–Kendall–Roberts (JKR) model that is more suitable for soft matter was chosen for the calculation, according to previously reports [36,37]. The elemental composition of the $(TA/peptide)_n$ was characterized by X-ray photoelectron spectroscopy (Thermo-Electron ESCALAB 250). SEM (WM2017015, HITACHI) was used to observe the surface morphology at 3 kV, after sputtering with platinum (10 s). The water contact angles were tested by static sessile drop method with affiliated KRUSS DSA1 v1.80 analyzer.

2.5. Quantifying the deposited R6-BFP and R6-RGD in the $(TA/R6\text{-}RGD\&BFP)_n$ film

Instead of the unlabeled R6-RGD and R6-BFP, the labeled R6-RGD-MCA and R6-BFP-TEMRA were used for constructing $(TA/R6\text{-}RGD\&BFP)_n$ film in the dark, with the mixed mass ratio of R6-RGD-MCA to R6-BFP-TEMRA at 5:5, 8:2, and 3:7. The amount of the deposited R6-BFP and R6-RGD in the $(TA/R6\text{- }RGD\&BFP)_n$ film was quantified by laser scanning confocal microscope (LSCM) (A1, Nikon) and UV–vis spectrophotometer, based on their standard curves. In brief, the fluorescence distribution before and after assembly was monitored under laser confocal microscopy to determine the peptide distribution. The fluorescence intensity was fitted by ImageJ software. Standard curves of the two fluorescently labeled peptides were measured separately using UV–visible near-infrared spectroscopy. The peptides adsorbed on the interfaces of different proportions of mixed peptides were quantified by measuring the absorbance of different proportions of the remaining fluorescent peptides in the solution before and after assembly and using the standard curves.

2.6. Cell culture, cellular migration, cellular adhesion and spreading at early stage

MC3T3-E1 purchased from Punosi was cultured in α-MEM medium supplemented with 100 mg/mL streptomycin, 100 U/mL penicillin, and 10 % FBS, with 5 % carbon dioxide at 37 °C. The MC3T3-E1 was passage until the coverage over 80 %. 4×10^4 MC3T3-E1 cells were seeded in 24-well sized glass or glass covered with $(TA/R6\text{-}RGD)_6$, $(TA/R6\text{- }BFP)_6$, and $(TA/R6\text{-}RGD\&BFP)_6$. After coverage over 80 %, a sterile 100-μL pipette tip was used to scratch on the slides. After washing with PBS, serum-free medium was place for another 24 h culture and the cell images were recorded by inverted fluorescence microscope. 2×10^4 MC3T3-E1 cells were seeded in 24-well sized glass or glass covered with $(TA/R6\text{-}RGD)_6$, $(TA/R6\text{- }BFP)_6$, and $(TA/R6\text{-}RGD\&BFP)_6$. After culturing 2 h and 4 h, the cells were fixed with 4 % paraformaldehyde, then treated by 0.1 % TritonX-100. The cytoskeleton and nuclei were then stained with rhodamine (red) and DAPI (blue), respectively, then recorded by CLSM (A1, Nikon). The analysis on the cellular numbers and cellular area were assisted by using Image J.

2.7. The force of cellular attachment on TA/RGD, TA/BFP, and TA/RGD&BFP films

2.5×10^4 MC3T3-E1 cells were seeded in 24-well sized glass or glass covered with $(TA/R6\text{-}RGD)_6$, $(TA/R6\text{- }BFP)_6$, and $(TA/R6\text{-}RGD\&BFP)_6$. After culturing for 12 h, the plates were centrifuged at 150 rpm for 30 min, then washed by PBS. The cell viabilities of each sample were detected using the CCK8 kit.

2.8. Cell viability and proliferation

1.0×10^4 MC3T3-E1 cells were seeded in 24-well sized glass or glass covered with $(TA/R6\text{-}RGD)_6$, $(TA/R6\text{-}BFP)_6$, and $(TA/R6\text{-}RGD\&BFP)_6$ and cultured for 7 days. The culture medium was refreshed in every 2 days. The cell viability was tested using a CCK8 kit on day 1, 3 and 7. Cells cultured at day 3 were fixed using paraformaldehyde, then treated by 0.1 % Triton X-100. The nucleus and cytoskeleton were stained with DAPI (blue) and rhodamine (red), respectively, then observed under CLSM.

2.9. Intracellular ROS scavenging

1.0×10^4 MC3T3-E1 cells were seeded in 24-well sized glass or glass covered with $(TA/R6\text{-}RGD)_6$, $(TA/R6\text{-}BFP)_6$, and $(TA/R6\text{-}RGD\&BFP)_6$ and cultured for 24 h. The culture medium was refreshed with 300 μM H_2O_2. After another 12 h culture, the DCFH-D (green), a detector of intracellular ROS, was added. After another 20 min incubation, cells were fixed using paraformaldehyde, then treated by 0.1 % Triton X-100. The nucleus and cytoskeleton were stained with DAPI (blue) and rhodamine (red), respectively, then observed under CLSM. The fluorescence intensity of ROS detector (DCFH-D, green) cell area and number of cells before and after H_2O_2 stimulation were analyzed with assistance of Image J.

2.10. Osteogenic staining analysis

2.0×10^4 MC3T3-E1 cells were seeded in 24-well sized glass or glass covered with $(TA/R6\text{-}RGD)_6$, $(TA/R6\text{- }BFP)_6$, and $(TA/R6\text{-}RGD\&BFP)_6$. At days 7 and 14, cells were fixed with 4 % paraformaldehyde. ALP activity was then detected using the BCIP/NBT kit and visualized using a microscope. On days 14 and 21, the calcium nodules were stained with 0.1 % alizarin red S solution for 30 min (pH 4.2). After fixing with 4 % paraformaldehyde, the cells were washed with PBS three times, and incubated with 10 % cetylpyridinium chloride solution for 1 h to extract the stained alizarin red S. The absorbance of alizarin red S at 593 nm was measured to quantify the calcium nodules.

2.11. Osteogenic genes expression

2.0×10^4 MC3T3-E1 cells were seeded in 24-well sized glass or glass covered with $(TA/R6\text{-}RGD)_6$, $(TA/R6\text{-}BFP)_6$, and $(TA/R6\text{-}RGD\&BFP)_6$. After 14 days, the RNA was extracted using TRIzol reagent, with the provided instruction by manufacture. After the reverse transcription to cDNA by the PrimeScript RT kit, the expression levels of Col-I, RUNX2, OCN were measured by a Real-Time PCR system (LightCycler480, Roche, USA). The level of relative expression was normalized by the housekeeping gene β-Actin. The $2^{-\Delta\Delta CT}$ method was applied for results analysis. The sequence of related forward (F) and reverse (R) primers for osteogenesis-related genes were listed in the following: F (CATGTACGTTGCTATCCAGGC) and R (CTCCTTAATGTCACGCACGAT) for β-actin; F (TTCCAGACCAGCAGCACTC) and R (CAGCGTCAACACCATCATTC) for RUNX2; F (GTGACGAGTTGGCTGACC) and R (TGGAGAGGAGCAGAACTGG) for OCN; F (GGGGCAAGACAGTCATCGAA) and R (GAGGGAACCAGATTGGGGTG) for COL-1, and F (GCAGAAGCCGCCAACCTGTG) and R (CTGTCCTGAGCATCAGCATGAGTC) for ALP.

2.12. Implantation

Sixteen Sprague–Dawley rats (healthy, male, 8-weeks old, 270–300 g in weight) were randomly separated into 4 groups (Ti rod, Ti rod with coatings of $(TA/R6\text{-}RGD)_6$, $(TA/R6\text{- }BFP)_6$, and $(TA/R6\text{-}RGD\&BFP)_6$, 4 rats in each group. After anesthetized for 5 min by intraperitoneal injection of 2 % pentobarbital sodium (Sigma Aldrich, USA) with a dosage of 3 mL/kg, the hind limb was shaved and fixed in the supine position. The longitudinal skin incisions were made by scissor, and a cylindrical hole with diameter 1.2 mm and length 10 mm was drilled in the direction of the major axis of femur. The Ti rods (with diameter 1.0 mm) without/with the coatings were insert into the hole. The soft tissues were closed, and the skin was sutured. After 5 or 8weeks, the rats were sacrificed in CO_2 incubator, and the bilateral femurs were dissected and fixed in 4 % paraformaldehyde for the following test.

All protocols involved in animal models were approved by the Wenzhou Institute of University of Chinese Academy Science with proved NO. WIUCASQD2019009. All procedures were performed according to the standard guidelines described in the Guide for the Care and Use of Laboratory Animals.

2.13. Analysis of microcomputed tomography (Micro-CT)

The dissected distal femur was photoed under micro-CT, with the parameters: current, 300 mA; voltage, 80 kV; and 360° rotation with a 0.5° rotation step. The region of interest around the distal femur was reconstructed, and the volume of new bone (BV) and total volume of bone (TV), data about trabecular were obtained by the affiliated software (CTAn and CTVol).

2.14. Pullout test

The binding strength between bone and implant was tested using the pushout experiment. Mounting the dissected distal femur on an Instron E10000 (Instron, USA) equipped with a 500-N manometer, and the titanium rod was pulled out from the bone tissue at a displacement rate of 1 mm/min until complete separation. The force-distance curves were recorded and the force of pullout was generated by the affiliated software.

2.15. Histology and histomorphometry

The dissected distal femur with implants were fixed with paraformaldehyde, washed by water, dehydrated by ethanol, immersed into xylene, then embedded in polymethyl methacrylate. The embedded tissue was sliced about 10-μm in thickness perpendicular with the direction of the long axis of the implant by a hard tissue slicer (EXAKT400CS). After stained with toluidine blue, The samples were maged under optical microscope (OLYMPUSBX43). The percentage of contact between bone and implant (BIC, the percentage of implant perimeter in direct contact with bone tissue) could be generated by Image-Pro Plus software.

2.16. Statistical analyses

All reported data are the average value of at least three duplicates, and the standard deviation was added as the error bar. For analyzing numbers of cells and cellular area, at least 10 images were randomly selected and analyzed using Image J (Official website, https://imagej.net/downloads). The graphical representation was done using Origin 2023b (OriginLab, MASS, USA). With GraphPad Prism 9.5 (GraphPad Software Inc., CA, USA), statistical analyses were performed using single-factor analysis of variance (ANOVA) and two-factor ANOVA for comparisons. The significance was noted as * $p < 0.05$, ** $p < 0.01$, and # $p < 0.001$.

3. Results and discussion

3.1. Fabrication of TA/peptide films

The TA/peptide films were obtained by a typical LBL process [38], with TA as the first layer and following by peptide deposition. The process of LBL TA/peptide was investigated under different pH, by testing the thickness. As shown in Fig. 1A, all TA/peptide films displayed linear growth with the numbers of deposited bilayers (or the cycles). The dependence of thickness of assembled pH was very similar to each other (Fig. 1A), with the thickest film obtained at pH 7.0. Increased pH (pH 8.5) or the decreased pH (pH 5.5) resulted in a decreased thickness. This was mainly attributed to the electrostatic interactions between TA and assembled unit R6. The pKa1 and pKa2 of TA are about 3.3 and 8.7, respectively [39]. At pH 5.5, partial phenol groups in TA were deprotonated, and more TA was negatively charged with increased pH, which contributed to the increased thickness from pH 5.5 to pH 7. From pH 7 to pH 8.5, the positive charges of R6 decreased. The two mutual constraints lead to the thickest film obtained at pH 7.0. The deposition process of TA/peptide films at pH 7.0 could be monitored by QCM-D technique. In Fig. 1B, the continuously decreased frequency and increased dissipation with the injecting cycle of TA and peptides, suggested the successful deposition of TA and peptides. With the assistance of the Voigt viscoelastic model, the thickness obtained by QCM-D was displayed in Fig. 1C. Similar growth trends to that in Fig. 1A, were observed. But the thickness obtained from QCM-D was higher than that tested by ellipsometer, due to the hydrated state of film tested in QCM-D [40]. The real-time deposition curves of peptides on $(TA/peptide)_{3.5}$ were extracted and showed in Fig. 1D, to better study the deposition behaviors of peptides. All these peptides exhibited similar deposited curves. And the values of characteristic times (T) during deposition of peptides were generated by fitting the kinetic equation and displayed in Fig. 1E. These values were very to each other, indicating the similar deposition kinetics of R6-RGD, R6-BFP, and R6-RGD&BFP on $(TA/peptide)_{3.5}$. These data in Fig. 1 strongly suggested the driving force of TA/peptide was derived from interactions between TA and R6. The stability of the coating is an important factor in the efficacy and longevity of bone implants. In particular, the long-term stability of the coating is a significant predictor of successful bone regeneration. The stability of $(TA/peptide)_6$ was tested by soaking into PBS, DMEM with or without proteinase K. As shown in Fig. 1F–H, the $(TA/peptide)_6$ coatings demonstrated overall stability over the 21-day testing period, with lost thickness less than 8 %. Specifically, less than 5 % of the coating thickness was lost in PBS. Conversely, the coating thickness increased by approximately 6 % in DMEM, while less than 8 % was lost in DMEM that also contained protease. The observed increase in the coating thickness may be attributed to the diffusion of amino acids into the coating. The enzymatic activity of proteases resulted in a higher rate of coating degradation than that observed in PBS. The presence of proteases is more closely aligned with the in vivo environment. It was fortunate, however, that the thickness of the coating was not significantly diminished. Compared to a previous report on the peptide coating constructed from TA and Lys6 linked functional peptides, which showed gradually decreased thickness in tested period and about 20 % loss after soaking into PBS for 21 days [29], the stability of the coatings in this study was much more robust. This might be attributed to the resistance of enzymatic degradation of BPF1 and the robust interaction between polyphenols and side chains of arginine, which served to impede the degradation of the coating by proteases.

In XPS spectra of $(TA/peptide)_6$, the appearance of N1s signal (Fig. 2A), sourced only from peptide, strongly supported the successful deposition of $(TA/peptide)_6$. Chemical composition of film was an important factor for biological application. And the composition based on the XPS data can be obtained. As shown in Fig. 2B, the peptide in $(TA/peptide)_6$ was about 41.7 %, 43.5 %, and 42.2 % for R6-RGD, R6-BFP, and R6-RGD&BFP, respectively. Similar as the composition

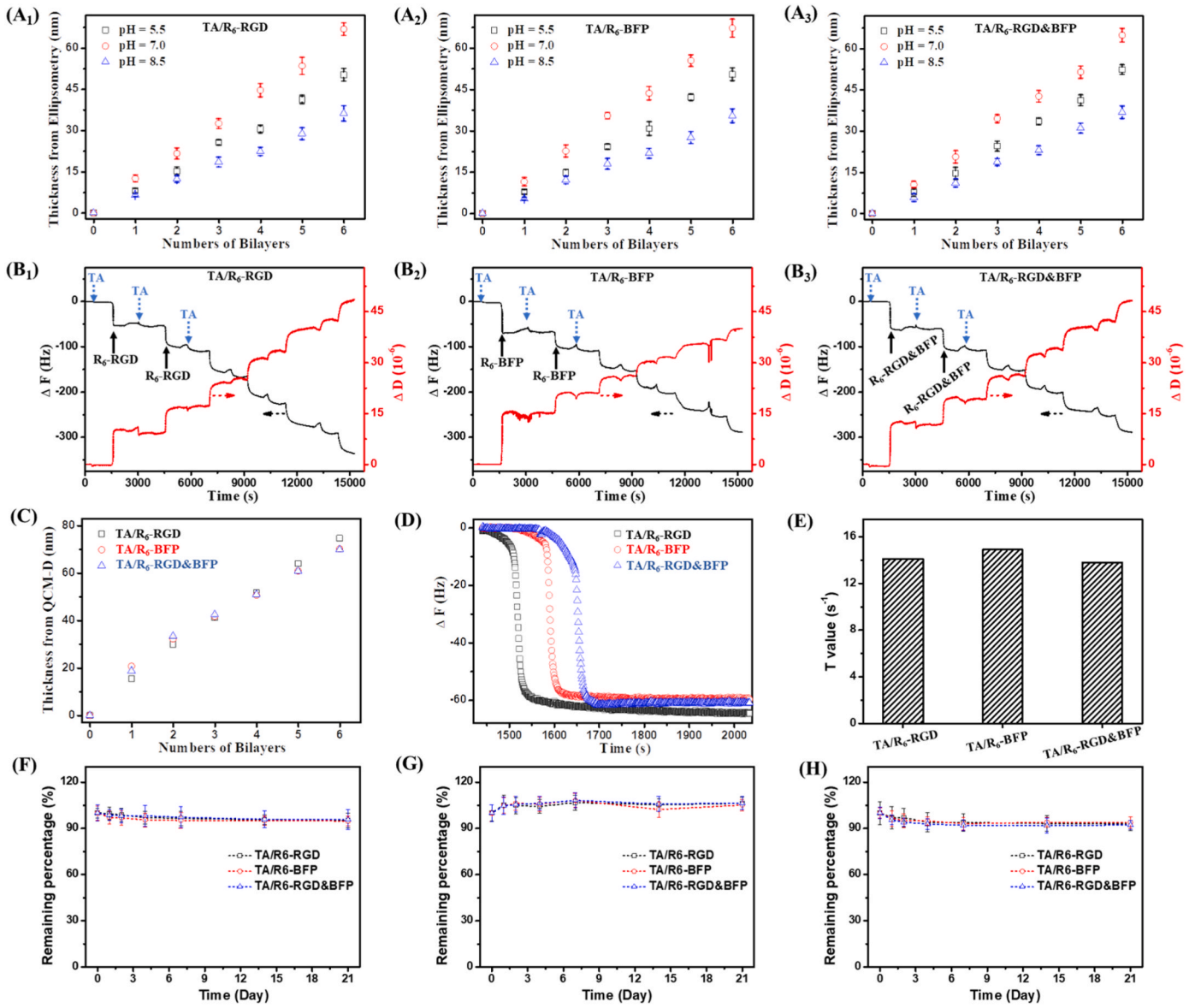

Fig. 1. The LBL process of TA/peptide. pH effect on the dependence of (A) TA/peptide thickness on the numbers of bilayers, (A1) TA/R6-RGD, (A2) TA/R6-BFP, and (A3) TA/R6-RGD&BFP; (B) The monitored growth of TA/peptide in real time by QCM-D, (B1) TA/R6-RGD, (B2) TA/R6-BFP, and (B3) TA/R6-RGD&BFP LBL at pH 7; (C) The thickness of TA/peptide generated from the QCM-D, by fitting with Voigt viscoelastic model. (D) The reported deposition curves of peptides onto the film of $(TA/peptide)_{3.5}$ by QCM-D. (E) The kinetic constants of peptide deposition onto the film of $(TA/peptide)_{3.5}$. The remaining percentage of $(TA/peptide)_6$ on silicon after soaking into (F) PBS, (G) DMEM without proteinase K and (H) DMEM with proteinase K.

obtained from the XPS, the data composition derived from QCM-D was displayed in Fig. 2C. To visualize the deposited peptide, the R6-RGD and R6-BFP was dyed with MCA (blue color) and TAMRA (red color), respectively. To show the power on modulating the composition and quantify the amounts of deposited peptides, RGD-MCA and BFP-TAMRA with different added ratios were used for the generation of $(TA/RGD\text{-}MCA\&BFP\text{-}TAMRA)_6$, which was imaged under LSCM. As shown in Fig. 2D, the brighter blue color was observed with the increased portion of RGD-MCA in mixture, while the brighter red color was observed with the increased portion of BFP-TAMRA. The fluorescent densities of RGD-MCA and BFP-TAMRA was measured with assistance of Image J., and showed in Fig. 2E, vividly illustrated above phenomena. The amount of deposited RGD-MCA and BFP-TAMRA could be quantified. As shown in Fig. 2F, at the ratios of RGD-MCA to BFP-TAMRA 2:8, 5:5 and 8:2, the deposited amounts of RGD-MCA vs BFP-TAMRA were 2.52 μg vs 13.25 μg, 9.19 μg vs 9.37 μg, and 13.14 μg vs 3.38 μg, respectively. Obviously, the deposited amounts of RGD-MCA to BFP-TAMRA were very close to the added ratios in mixture solution. These data indicated the deposited peptide onto the TA/peptide films could be easily controlled by the added amount into the mixture of R6-RGD and R6-BFP, benefiting from the same driving force during the deposition of R6.

Considering the morphology and stiffness are two of the most significant factors on cellular behaviors [41], the morphology and stiffness of $(TA/peptide)_6$ were investigated under liquid environment. All $(TA/peptide)_6$ showed the similar morphologies, sphere particles assembled from TA and peptide, distributed evenly throughout whole scanned area (Fig. 3A). And the roughness of $(TA/peptide)_6$ showed decreased trend from TA/R6-RGD, TA/R6-BFP, to TA/R6-RGD&BFP, without no big difference (Fig. 3B). In the observation of SEM (Fig. 3C), all $(TA/peptide)_6$ showed the similar morphologies as tested by AFM (Fig. 3A). The water drops showed the spread shapes for all $(TA/peptide)_6$ samples, as photoed in (Fig. 3D). The values of water contact angle (WCA) of $(TA/R6\text{-}RGD)_6$, $(TA/R6\text{-}BFP)_6$ and $(TA/R6\text{-}RGD\&BFP)_6$ were about 19.8 ± 0.5^0, 51 ± 2.2^0, and 45 ± 1.9^0, respectively (Fig. 3E). The

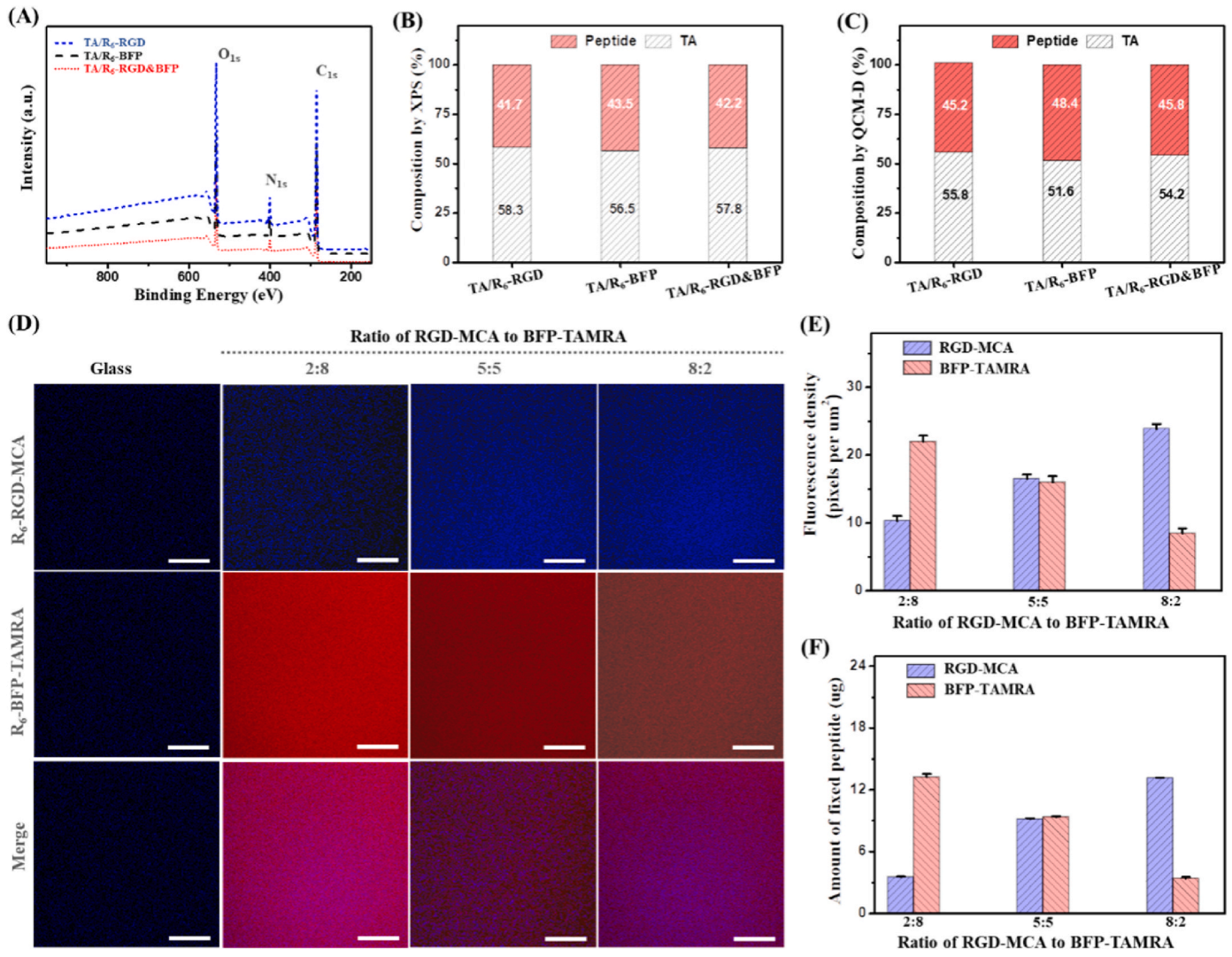

Fig. 2. Quantitative analysis on the component of peptide in the film of $(TA/peptide)_6$. (A) The XPS curves of $(TA/peptide)_6$. The composition of $(TA/peptide)_6$ tested by (B) XPS and (C) QCM-D. (D) Fluorescence photographs of $(TA/RGD\text{-}MCA\&BFP\text{-}TAMRA)_6$ under the channels of blue (RGD-MCA) and red (BFP-TAMRA) respectively, (E) the fluorescence density of RGD-MCA and BFP-TAMRA (F) the amount of fixed peptide in $(TA/RGD\text{-}MCA\&BFP\text{-}TAMRA)_6$ at the ratios of RGD-MCA to BFP-TAMRA 2:8, 5:5 and 8:2. The scale bar in (D) is 100 μm.

modulus maps (Fig. 3F, top panel) and distributions (Fig. 3F, bottom panel) of $(TA/peptide)_6$ were displayed in (Fig. 3F), and the values of Young's modulus of TA/R6-RGD, TA/R6-BFP, and TA/R6-RGD&BFP were generated (Fig. 3G) by affiliated software, in which no significant difference was observed. It has to be noted, the modulus of $(TA/peptide)_6$ is much higher than the modulus from classic LBL polyelectrolyte multilayers (PEMs) prepared by alternative deposition positively charged polyelectrolyte and negatively charged polyelectrolyte, which was in the range of tens to hundreds of kPa, relying on the concentration of added crosslinker [42]. For example, Picart et al. [43]. tested the modulus of PEMs composed of poly(L-lysine) and hyaluronan by AFM in liquid, they found that the modulus of native film was about 20 kPa, and increased to 800 kPa after crosslinking by EDC/NHS. As reported, the modulus of PEMs could be influenced by chain conformation and the charge density of applied polyelectrolytes, the preparing conditions, the crosslinking density, components incorporated into PEMs, tested environment and method, data processing, etc., which made it hard to exactly compare the obtained results one by one [43,44]. The multiple interactions between TA and R6 peptide attributed to the high modulus of (TA/peptide)6, which serves as the high crosslinking density. Such high modulus is beneficial for the osteogenesis of bone marrow stem cells [45].

3.2. Cellular behaviors of attachment, migration, and proliferation on $(TA/peptide)_6$ films

It is of paramount importance that the cells adhere to the implant as soon as they are implanted in the body, as this reduces the risk of infection. Since the space on the implant surface is limited, the sooner the cells occupy the implant surface, the less room is left for bacterial infection [46]. The cellular attachment at early stage was investigated by seeding MC3T3-E1 onto $(TA/peptide)_6$ films [46]. After 2h and 4h incubation, the attached cells were imaged and showed in Fig. 4A, in which the number and spread area of attached cells on $(TA/peptide)_6$ films were obviously higher than that in the positive control (glass, a cell-friendly substrate). The quantitative analysis of number of attached cells and spreading area per cell at 2 h and 4 h were carried out and displayed in (Fig. 4B and C), respectively. Compared to control, all $(TA/peptide)_6$ films exhibited significant increase in the number of attached cells and spreading area per cell at 2 h and 4 h. Among the three $(TA/peptide)_6$ films, $(TA/R6\text{-}RGD\&BFP)_6$ film showed the highest cellular attachment and spreading area per cell, while the $(TA/R6\text{-}BFP)_6$ film had the least cellular attachment and spreading area per cell, at all tested time points (2 h and 4 h). This indicated the anchoring of RGD was beneficial to the cellular attachment and spreading, which was

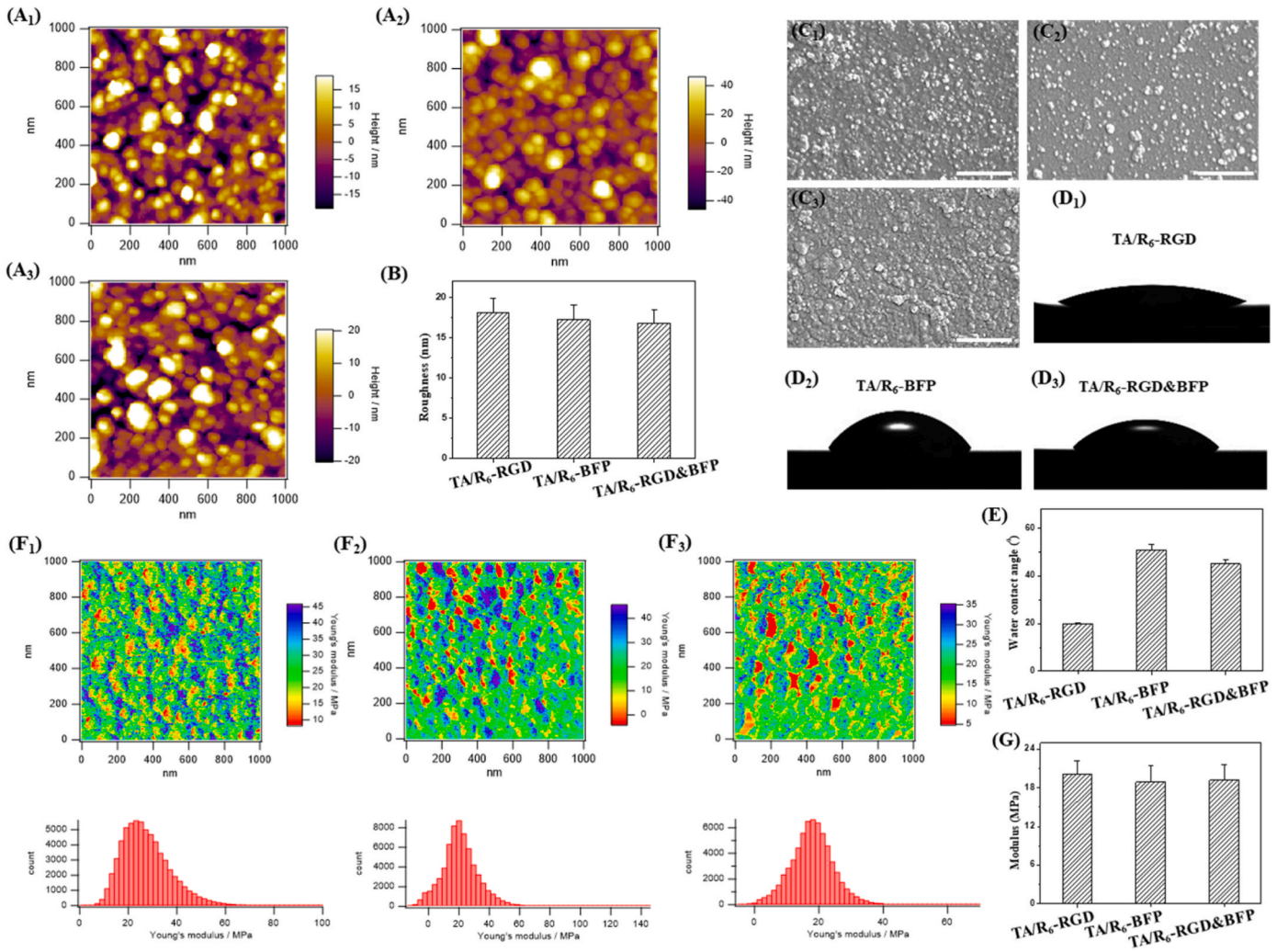

Fig. 3. The morphology and mechanical properties of the $(TA/peptide)_6$. (A) The topographies and (B) the roughness $(TA/peptide)_6$ in liquid state tested by AFM. (C) The SEM images and (D) photos of water drop on $(TA/peptide)_6$. (E) The water contact of $(TA/peptide)_6$. (F) The modulus map (top) and modulus distribution (bottom), and (G) the modulus of $(TA/peptide)_6$ in liquid state, as tested by AFM. The scale bar in D was 500 nm.

consistent with previous reports [47]. Another proof in the RGD effect on cellular attachment was the experiment of cell viability or the numbers of left cells after shear force (Fig. 4D). After seeding MC3T3-E1 onto $(TA/peptide)_6$ films for 12 h, the plates were centrifuged at 150 rpm for 30 min, the cell viabilities on $(TA/R6\text{-}RG)_6$, and $(TA/R6\text{-}RGD\&BFP)_6$ were comparable to that on glass, and higher than that on $(TA/R6\ BFP)_6$ (Fig. 4D), suggesting the fixed RGD was helpful to cell attachment.

Cell migration refers to the movement of cells after receiving a migration signal or feeling the migration cues integrated with substances. Cell migration is one of the basic functions of normal cells, a physiological process for the normal growth and development of the body, and a form of movement that is ubiquitous in living cells [48]. For the bone implants, the fast migration is good to the bone regeneration [49]. To evaluate the effect of the fixed peptides on cellular migration, the scratches were carefully made on the MC3T3-E1 cells sheet cultured for 24 h, the cells were imaged before (Fig. 4E, top) and after (Fig. 4E, bottom) another 24 h culture under free medium [50]. For all samples, the gaps two cell edges shrunk after 24 h. It seemed much smaller for $(TA/peptide)_6$ with fixed RGD samples: $(TA/R6\text{-}RGD)_6$ and $(TA/R6\text{-}RGD\&BFP)_6$ than $(TA/R6\text{-}BFP)_6$. The quantitative in the migration rate was showed in Fig. 4F, in which all $(TA/peptide)_6$ had much higher cellular migration rate than that on glass. There was no big difference between $(TA/R6\text{-}RGD)_6$ and $(TA/R6\text{-}RGD\&BFP)_6$, but much faster than that of $(TA/R6\text{-}\ BFP)_6$.

To evaluate the cellular proliferation on $(TA/peptide)_6$, MC3T3-E1 cells were cultured for 7 days and imaged in Fig. 4G, in which MC3T3-E1 cells were fully covered on all samples and it's hard to tell which one was better for cellular attachment. The cellular viabilities were tested at different time-points (1, 3, 7 days). As shown in Fig. 4H, the cell viabilities increased with the cultured days, indicating the cell proliferation processed normally. At all tested time-points, all $(TA/peptide)_6$ owned better cellular proliferation than that of glass. Among all $(TA/peptide)_6$, $(TA/R6\text{-}RGD)_6$ and $(TA/R6\text{-}RGD\&BFP)_6$ exhibited no big difference, but better cellular proliferation than that of $(TA/R6\text{-}BFP)_6$.

3.3. Antioxidant profile of $(TA/peptide)_6$

Reactive oxygen species (ROS), including non-radical species like hydrogen peroxide (H2O2), and free radicals such as the hydroxyl radical (•OH) and superoxide anion radical (O2•−), are generated at various organelles and considered as the second most significant signals in a variety of biological pathways [51]. High ROS concentration, ROS stress, happens once the antioxidant defenses was overwhelmed by the production of ROS. ROS stress damages to lipids, proteins, and nucleic acids, leading to various diseases [52]. Surrounding the implants, it's a ROS stress environment caused by the foreign material and trauma

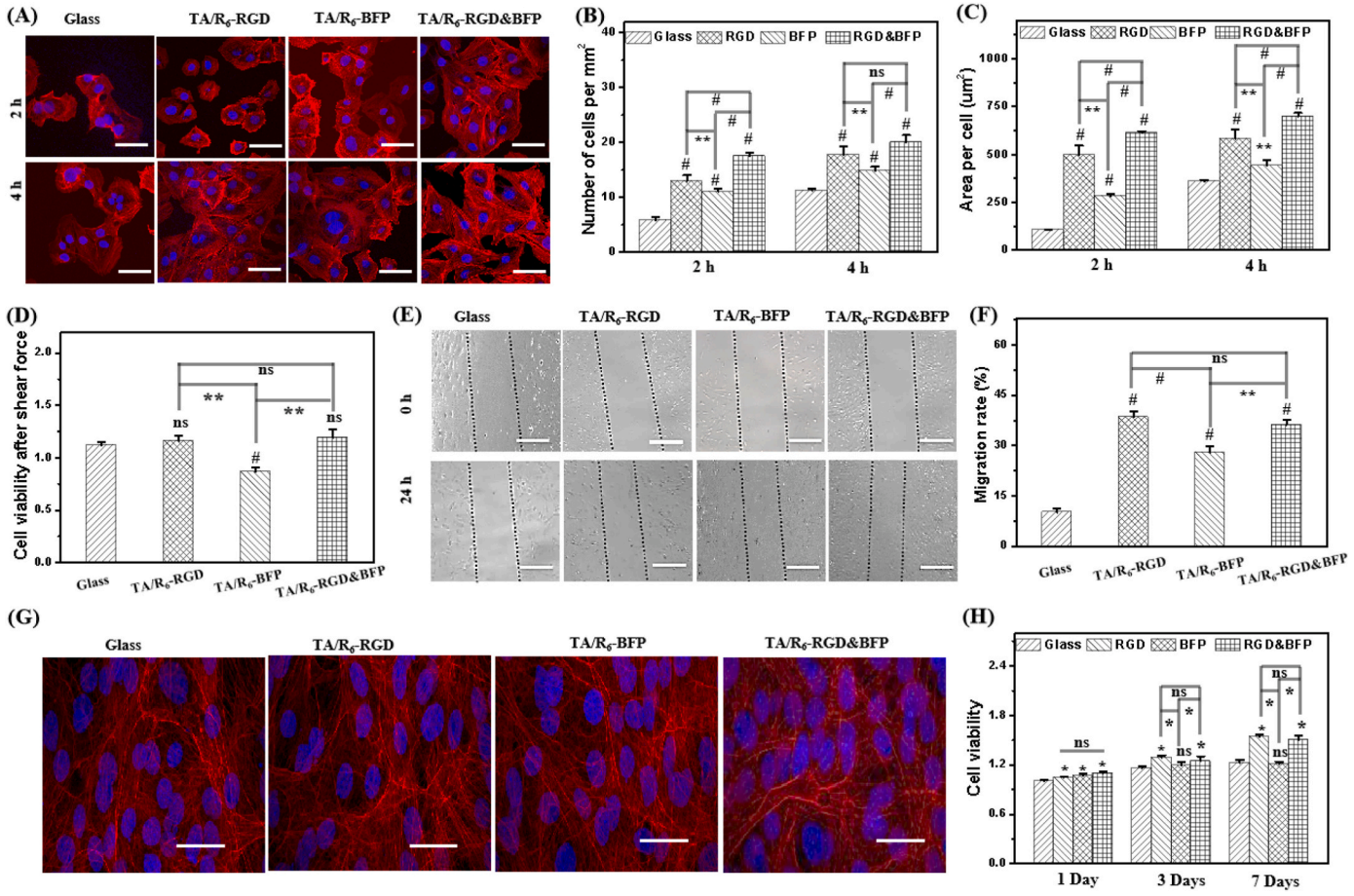

Fig. 4. Migration, attachment at early stage, adhesion, and proliferation of MC3T3-E1 cells on $(TA/peptide)_6$. (A) The fluorescent images of MC3T3-E1 cells, (B) Number of MC3T3-E1cells per mm^2 and (C) Area per cell after seeding at early stage on $(TA/peptide)_6$ for 2 h and 4 h. (D) The cell viability after shear force. (E) The microscopic images of MC3T3-E1 under the light field, with scratch (top) and after 24 h culture without serum supplement (bottom). (F) The migration rate of MC3T3-E1 on $(TA/peptide)_6$. (G) The fluorescent images of MC3T3-E1 cells at Day 7. (H) The dependence of cell viability of MC3T3-E1cells with the cultured days. The scale bar is 5 μm in (A) and (G), 50 μm in (E). The red color and blue color in fluorescent images are the actin cytoskeleton stained with rhodamine phalloidin and nuclei stained with DAPI of MC3T3-E1 cells.

fragments, which plays a negative role on osseointegration [53,54].It has been reported ROS stress can reduce the ability of cell attachment, rate of migration, and inhibit osteogenesis [53,54]. The antioxidant ability of the $(TA/peptide)_6$ was evaluated by adding H2O2 into the cell culture medium to mimic ROS stress environment. The cell images were shown in Fig. 5A, in which the shrink of cells attached on glass was obviously visualized (no antioxidant ability) and no obvious shrink of cells attached on $(TA/peptide)_6$ was observed. These observations could be strongly supported by quantitative analysis of the number of cells per mm^2 (Fig. 5B) and area per cell (Fig. 5C) before and after H2O2 stimulation. With the ROS reporter DCFH-D (green color), the color seemed increased for all samples after H2O2 stimulation, but the increased intensity of cells on glass was much higher than those on $(TA/peptide)_6$. Quantitative analysis on the mean fluorescent intensity (F. I.) was displayed in Fig. 5D–and a sharp increase for cells on glass after H2O2 stimulation. Although there was slight increase of mean F. I. for cells on $(TA/peptide)_6$ after H2O2 stimulation, there was no significant difference to that before H2O2 stimulation. Overall, all $(TA/peptide)_6$ exhibited strong antioxidant profile and maintaining the normal ROS levels in ROS stress environment.

3.4. *In vitro osteogenesis abilities of* $(TA/peptide)_6$

Alkaline phosphatase (ALP), a marker of osteogenesis at early stage, its expressed level is high in the cells of mineralized tissue and plays a critical role in the formation of bone tissue [55].Increased alkaline phosphatase levels generally indicate enhanced osteoblast activity and osteo-transition status, and are therefore considered a key factor required for fresh bone mineralization and synthesis [56]. The in vitro expressed ALP levels of MC3T3-E1 cells on glass and $(TA/peptide)_6$ were evaluated by ALP staining (blue color). After seeding MC3T3-E1 cells for 7 days and 14 days, the ALP staining images were displayed in Fig. 6A. Regardless at 7 or 14 days, the blue color of all $(TA/peptide)_6$ samples appeared darker than glass, and the color of $(TA/R6\text{-}RGD\&BFP)_6$ was the darkest in the $(TA/peptide)_6$ samples, followed by $(TA/R6\text{-}BFP)_6$, and then $(TA/R6\text{-}RG)_6$. And the quantitative analysis strongly proved the above appearance (Fig. 6B). Insoluble inorganic calcium salts are a normal component of bone in the later stages of bone formation, which could be stained by various dyes. The alizarin red S is considered the gold standard for the quantification of osteoblast mineralization and is therefore widely used in the study of calcium deposition [57]. After seeding MC3T3-E1 cells for 14 days and 21 days, the alizarin red S (red color) staining images were displayed in Fig. 6C. Judging from the colors observed, whether at 14 or 21 days, the amount of calcium deposition in all $(TA/peptide)_6$ samples is more than that of glass. Among all $(TA/peptide)_6$ samples, the amount of calcium deposition in $(TA/R6\text{-}RGD\&BFP)_6$ was the highest followed by $(TA/R6\text{-}BFP)_6$, and the least was $(TA/R6\text{-}RG)_6$. After extracting the stained alizarin red S, the amount of calcium deposition could be quantified and above observations were strongly supported (Fig. 6D).

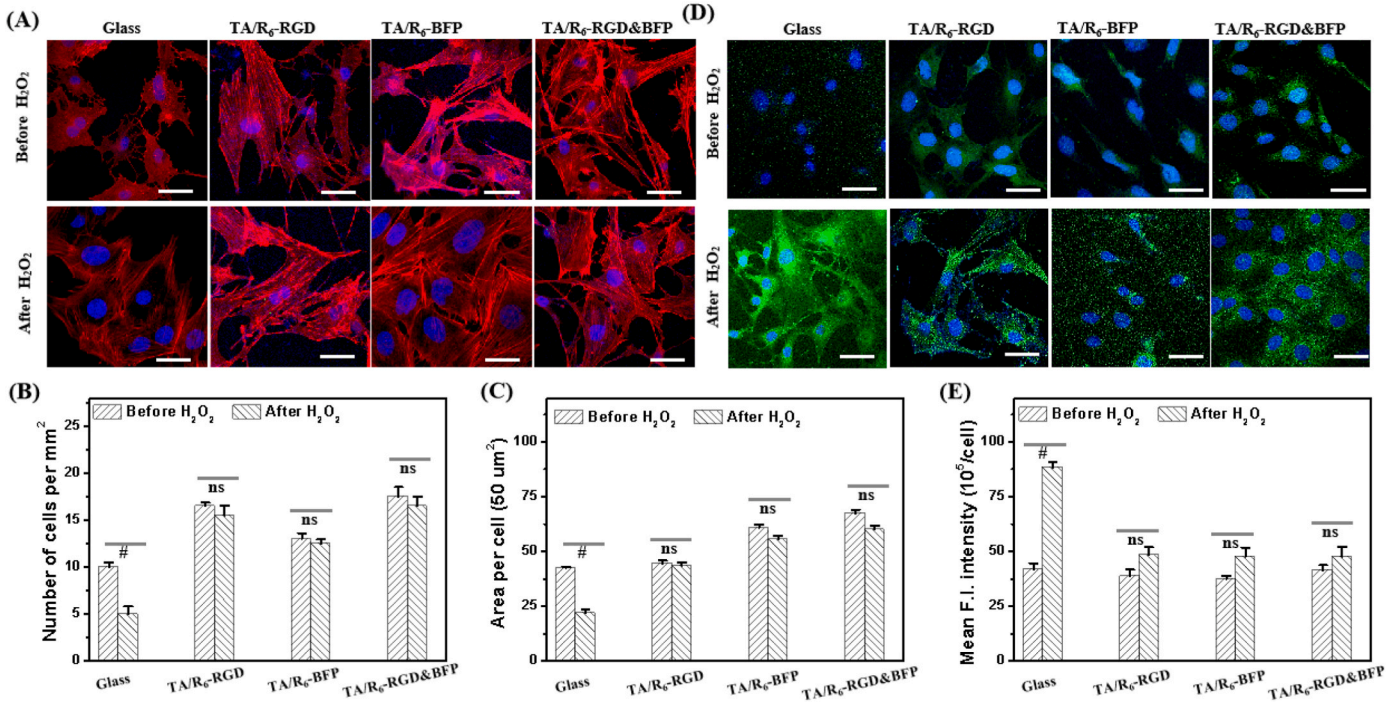

Fig. 5. The antioxidant performance of $(TA/peptide)_6$ with attached MC3T3-E1 cells under H2O2 stimulation. (A) Fluorescent images of MC3T3-E1 cells, (B) with the ROS reported by DCFH-D, (C) Number of cells per mm2, (D) Area per cell, and (E) Mean fluorescent intensity per cell before and after H_2O_2 stimulation. The scale bars are 10 μm in (A) and 20 μm in (D). In fluorescent images of MC3T3-E1 cells in (A) and (B), the red color is the actin cytoskeleton stained with rhodamine phalloidin, blue color is and nuclei stained with DAPI, and green color was the ROS reported by DCFH-D.

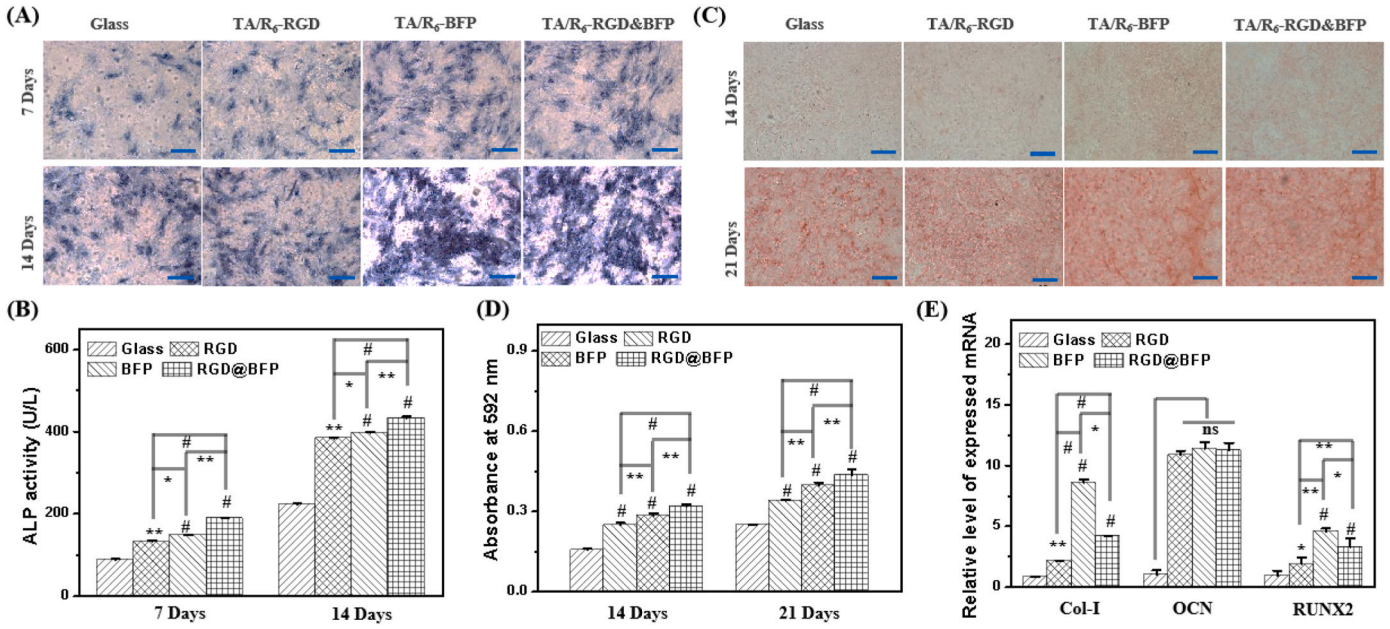

Fig. 6. The in vitro osteogenesis ability of $(TA/peptide)_6$. (A) ALP staining and (B) quantitative analysis on the ALP activities of MC3T3-E1 cells cultured on glass and $(TA/peptide)_6$ for 7 and 14 days. (C) The alizarin red S staining and (D) quantitative analysis on alizarin red S staining for MC3T3-E1 cells cultured on glass and $(TA/peptide)_6$ for 14 and 21 days. (E) Relative level of expressed mRNA of bone differentiation-related proteins (Col-I, OCN, and RUNX2) in MC3T3-E1 cells cultured on glass and $(TA/peptide)_6$ for 14 days. The scale bars in (A) and (C) are 100 μm.

Collagen type I, the dominant type of collagen and major organic component in bone tissue, forms the triple helices scaffold for bone cells and plays critical role in promoting bone formation and maintaining the bone strength [58]. Osteocalcin (OCN) produced by osteoblast, is the dominant non-collagenous protein in bone, was considered as a marker for bone formation and osteoblast activity [59]. Runt-related transcription factor 2 (RUNX2) is the first transcription factor required to determine the lineage of osteoblasts, and its expression levels are related to the maturity of osteoblasts, up-regulated in immature osteoblasts and down-regulated in mature osteoblasts [60]. To better understand the osteogenesis abilities of $(TA/peptide)_6$, the relative level of expressed mRNA of bone differentiation-related proteins (Col-I, OCN,

and RUNX2) in MC3T3-E1 cells cultured on glass and $(TA/peptide)_6$ for 14 days were tested by RT-qPCR technique [61]. Overall, the expression of all proteins (Col-I, OCN, and RUNX2) was higher on $(TA/peptide)_6$ samples than on glass, indicating better osteogenesis abilities of $(TA/peptide)_6$. For expressed level of OCN, these three $(TA/peptide)_6$ samples were comparable to each other. For the expressed level of Col-I and RUNX2, $(TA/R6\text{-}BFP)_6$ was the highest, followed by $(TA/R6\text{-}RGD\&BFP)_6$ and $(TA/R6\text{-}RGD)_6$, reflecting the strong ability of BFP as the bone formation peptide on osteogenesis.

3.5. *In vivo osteogenesis and osteointegration of $(TA/peptide)_6$*

The osteogenesis and osteointegration behaviors of $(TA/peptide)_6$ were investigated by the previously reported animal model [38,62,63], where bare Ti rod and Ti rod coated with $(TA/peptide)_6$ were implanted into rats' femur. After implanting for 4 and 8 weeks, the rats' femur was dissected and imaged under micro-CT. The representative 3D reconstructed micro-CT images of new bone attached on bare Ti rod and bare Ti rod coated with $(TA/peptide)_6$ after implanting for 4 weeks and 8 weeks were exhibited in Fig. 7A. At the same time point (4 weeks or 8 weeks), it seemed more bone was generated on Ti rod coated with $(TA/peptide)_6$ than that on bare Ti rod. Among the Ti rod coated with $(TA/peptide)_6$, $(TA/R6\text{-}RGD\&BFP)_6$ seemed receiving highest amount of bone formation, followed by $(TA/R6\text{-}BFP)_6$ and $(TA/R6\text{-}RGD)_6$. The quantitatively analyzed bone volume fraction (BV/TV) found that the BV/TV values of rod coated with $(TA/peptide)_6$, were much higher than that of bare rod (Fig. 7B). But, no matter at 4 weeks or 8 weeks, the BV/TV values of $(TA/R6\text{-}BFP)_6$ and $(TA/R6\text{-}RGD\&BFP)_6$ showed no big difference between each other, but higher than that of $(TA/R6\text{-}RGD)_6$ (Fig. 7B). Trabecular bone (Tb.) is an extension of cortical bone within cancellous bone and is important for microstructural analysis of trabecular bone [64]. Therefore, the trabecular number (Tb.N), trabecular thickness (Tb.Th) and trabecular separation (Tb.Sp) were analyzed and displayed in Fig. 7C–E, respectively. Compared to bare Ti rod, all parameters related to trabecular of Ti rod coated with $(TA/peptide)_6$ were significantly high (Fig. 7C–E). Among the coatings, $(TA/R6\text{-}RGD\&BFP)_6$ had the biggest values in Tb.N, Tb.Th, and Tb.Sp, followed by $(TA/R6\text{-}BFP)_6$ and $(TA/R6\text{-}RGD)_6$. The pullout force is another important parameter in evaluating the osteointegration between implant and bone tissue, good osteointegration means the high pullout force [65]. The pullout force was tested and exhibited in Fig. 7F. Regardless the implantation time (4 weeks and 8 weeks), the higher

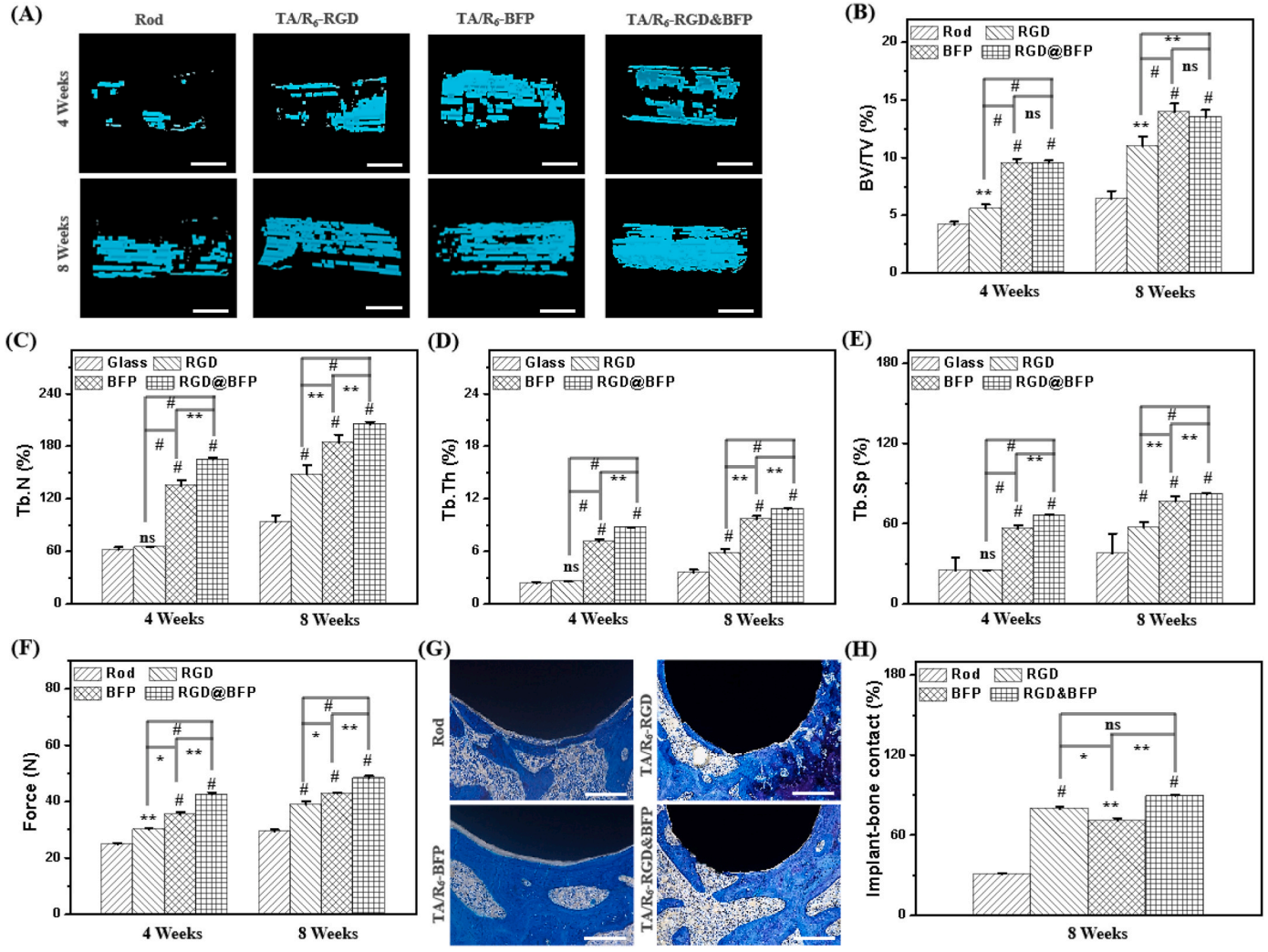

Fig. 7. The in vivo osteogenesis and osteointegration of $(TA/peptide)_6$. (A) The representative 3D reconstruction micro-CT images of new bone attached on bare Ti rod and bare Ti rod coated with $(TA/peptide)_6$ after implanting for 4 weeks and 8 weeks. The quantitatively analyzed (B) bone volume fraction (BV/TV), (C) trabecular number (Tb. N), (D) trabecular thickness (Tb.Th) and (E) trabecular separation (Tb.Sp) based on the images in (A). (F) The average pullout force. Of the bare Ti rod coated with $(TA/peptide)_6$ after implanting for 4 weeks and 8 weeks. (G) Representative histological images stained with toluidine blue (the scale bar is 100 μm) of bare Ti rod and bare Ti rod coated with $(TA/peptide)_6$ after implanting for 8 weeks. (H) Average values of implant-bone contact (IBC) based on images in (G). The scale bars in (A) and (G) were 2 mm and 500 μm, respectively.

force was needed to pullout Ti rod coated with $(TA/peptide)_6$ than that of bare Ti rod (Fig. 7F). Comparing between Ti rod coated with $(TA/peptide)_6$, $(TA/R6\text{-}RGD\&BFP)_6$ needed greatest force followed by $(TA/R6\text{-}BFP)_6$ and $(TA/R6\text{-}RGD)_6$ (Fig. 7F). The osteointegration could be further investigated by the histological images stained with toluidine blue (Fig. 7G). More implant-bone contact (IBC) suggests better osteointegration. The value of BIC was counted and displayed in Fig. 7H. All Ti rod coated with $(TA/peptide)_6$ had higher BIC values than that of bare Ti rod. For Ti rod coated with $(TA/peptide)_6$, the BIC value of $(TA/R6\text{-}RGD\&BFP)_6$ was comparable to that of $(TA/R6\text{-}RGD)_6$, both of which were significantly higher that of $(TA/R6\text{-}BFP)_6$. Gathering all in vivo data, anchoring RGD was helpful to increase the contact between bone tissue and implant, and fixation of BFP was beneficial to the bone formation and osteointegration. Most importantly, the mixed coating of RGD&BFP performed the best in the bone formation, increasing BIC and osteointegration.

The process of osseointegration is characterized by the involvement of multiple cells and multiple signaling factors. The construction of multifunctional coatings to provide the necessary biological factors for the osseointegration process is an effective strategy to improve the osseointegration ability of implants. Based on this, multifunctional coatings prepared by coupling two or more elements of the osseointegration process have been widely reported [66,67], such as combining antimicrobials and osteogenesis, angiogenesis and osteogenesis. In our work, we integrated two key elements of the osseointegration process, i.e., cell adhesion (RGD) and bone morphogenetic protein (BFP), into an implant coating, expecting to achieve the colonization of bone marrow stem cells, osteoblasts, etc., on the implant surface by using RGD, and to increase the bone regeneration capacity by using BFP. Our results show that the coating of bifunctional peptides is better than the coating of monofunctional peptides both in promoting cell adhesion and osteogenic differentiation in vitro and in osteointegration of the implant in vivo. This result highlights the need for a multifunctional coating during implant osseointegration.

Another contribution of our work is to provide a strategy for the presentation of functional peptides on the surface of implants. The main advantages of this strategy include mild preparation conditions, ease of manipulation, simultaneous display of different functional peptides on the surface, etc. In contrast to conventional LBL assembly techniques, functional peptides often have to be chemically coupled to polyelectrolytes and then the peptide-modified polyelectrolytes are assembled LBL [68]. The resulting coatings can hardly achieve the required peptide density for osseointegration (normally, the content of peptide less than 10 % [30]). In addition, entanglement and osmotic diffusion of the polyelectrolyte during the assembly process can easily bury the peptide inside the polyelectrolyte coating, leading to the effective performance of its biological function. In this strategy, peptide presentation based on small molecule LBL assembly avoids the defect of functional peptides being embedded in the coating and greatly increases the peptide content in the coating (content of peptide more than 40 %).

4. Conclusions

In summary, we successfully engineered solo-peptide (TA/R6-RGD, or TA/R6-BFP) and dual-peptides functionalized (TA/R6-RGD&BFP) coatings, which exhibited good stability in a variety of solution environments, with thickness linearly dependent on the numbers of LBL cycles. The same driving force between assembly fragments lead to the similar deposition kinetics and deposition processes of R6-RGD, R6-BFP, and R6-RGD&BFP coatings. The chemical composition of the TA/R6-RGD&BFP could be easily controlled, consistent with the composition of the R6-RGD&BFP in the assembly solution. The coating had a higher mechanical modulus than the polyelectrolyte multilayer film. These coatings had excellent biological behavior in vivo and in vitro. Compared with single-functional peptide coatings (TA/R6-RGD, or TA/R6-BFP), bifunctional peptide coatings (TA/R6-RGD&BFP) exhibited rapid early cell adhesion, faster cell proliferation and better differentiation of bone-related genes, and better antioxidant capacity. In in vivo animal model experiments, the dual-peptides functionalized coating had higher bone formation, higher values of pullout force, Tb.N, Tb.Th and Tb.Sp. These results will provide new ideas for the design of multifunctional coatings that can cope with the complex bone regeneration process and improve the osseointegration ability of implants.

CRediT authorship contribution statement

Hui Nan: Writing – original draft, Methodology, Formal analysis, Conceptualization. **Yong Gou:** Methodology. **Chunkai Bao:** Methodology. **Hangjin Zhou:** Formal analysis. **Haoran Qian:** Formal analysis. **Xingjie Zan:** Writing – review & editing. **Lianxin Li:** Writing – review & editing, Funding acquisition. **Enxing Xue:** Writing – review & editing, Funding acquisition, Conceptualization.

Declaration of competing interest

The authors declare that they have no known competing financial interests or personal relationships that could have appeared to influence the work reported in this paper.

Data availability

The data that has been used is confidential.

Acknowledgement

This work was financially supported by Natural Science Foundation of Zhejiang Province (LY20H060004) and Shandong Province Major Scientific and Technical Innovation Project (No. 2021SFGC0502).

References

[1] N.E. Putra, J. Zhou, A.A. Zadpoor, Sustainable sources of raw materials for additive manufacturing of bone-substituting biomaterials, Adv. Healthcare Mater. (2023) e2301837, https://doi.org/10.1002/adhm.202301837.
[2] N.P. Lang, B.E. Pjetursson, K. Tan, U. Bragger, M. Egger, M. Zwahlen, A systematic review of the survival and complication rates of fixed partial dentures (FPDs) after an observation period of at least 5 years. II. Combined tooth–implant-supported FPDs, Clin. Oral Implants Res. 15 (2004) 643–653.
[3] J.G. Werny, K. Sagheb, L. Diaz, P.W. Kämmerer, B. Al-Nawas, E. Schiegnitz, Does vitamin D have an effect on osseointegration of dental implants? A systematic review, Int. J. Implant Dent. 8 (2022) 16.
[4] A.F. Mavrogenis, R. Dimitriou, J. Parvizi, G.C. Babis, Biology of implant osseointegration, J. Musculoskelet. Neuronal Interact. 9 (2009) 61–71.
[5] A.L. Overmann, C. Aparicio, J.T. Richards, I. Mutreja, N.G. Fischer, S.M. Wade, B. K. Potter, T.A. Davis, J.E. Bechtold, J.A. Forsberg, D. Dey, Orthopaedic osseointegration: implantology and future directions, J. Orthop. Res. 38 (2020) 1445–1454.
[6] F. Jia, D. Xu, Y. Sun, W. Jiang, H. Yang, A. Bian, Y. Liu, K. Liu, S. Zhang, Y. Wang, H. Qiao, H. Lin, J. Lan, Y. Huang, Strontium-calcium doped titanium dioxide nanotubes loaded with GL13K for promotion of antibacterial activity, anti-Inflammation, and vascularized bone regeneration, Ceram. Int. 49 (2023) 35703–35721.
[7] J.W.Y. Lee, M.L. Bance, Physiology of osseointegration, Otolaryngol. Clin. 52 (2019) 231–242.
[8] B. Wang, Y. Li, S. Wang, F. Jia, A. Bian, K. Wang, L. Xie, K. Yan, H. Qiao, H. Lin, J. Lan, Y. Huang, Electrodeposited dopamine/strontium-doped hydroxyapatite composite coating on pure zinc for anti-corrosion, antimicrobial and osteogenesis, Mater. Sci. Eng., C 129 (2021) 112387.
[9] J. Krieghoff, M. Gronbach, M. Schulz-Siegmund, M.C. Hacker, Biodegradable macromers for implant bulk and surface engineering, Biol. Chem. 402 (2021) 1357–1374.
[10] M. Morra, Biochemical modification of titanium surfaces: peptides and ECM proteins, Eur. Cell. Mater. 12 (2006) 1–15.
[11] I. Pountos, M. Panteli, A. Lampropoulos, E. Jones, G.M. Calori, P.V. Giannoudis, The role of peptides in bone healing and regeneration: a systematic review, BMC Med. 14 (2016) 103.
[12] N. Nun, A. Joy, Fabrication and bioactivity of peptide-conjugated biomaterial tissue engineering constructs, Macromol. Rapid Commun. 44 (2023) e2200342.
[13] W. Li, Y. Zheng, X. Zhao, Y. Ge, T. Chen, Y. Liu, Y. Zhou, Osteoinductive effects of free and immobilized bone forming peptide-1 on human adipose-derived stem cells, PLoS One 11 (2016) e0150294.

[14] M. Yang, Z.C. Zhang, Y. Liu, Y.R. Chen, R.H. Deng, Z.N. Zhang, J.K. Yu, F.Z. Yuan, Function and mechanism of RGD in bone and cartilage tissue engineering, Front. Bioeng. Biotechnol. 9 (2021) 773636.
[15] B. Wang, Z. Wu, S. Wang, S. Wang, Q. Niu, Y. Wu, F. Jia, A. Bian, L. Xie, H. Qiao, X. Chang, H. Lin, H. Zhang, Y. Huang, Mg/Cu-doped TiO(2) nanotube array: a novel dual-function system with self-antibacterial activity and excellent cell compatibility, Mater. Sci. Eng., C 128 (2021) 112322.
[16] B. Wang, Z. Wu, J. Lan, Y. Li, L. Xie, X. Huang, A. Zhang, H. Qiao, X. Chang, H. Lin, H. Zhang, T. Li, Y. Huang, Surface modification of titanium implants by silk fibroin/Ag co-functionalized strontium titanate nanotubes for inhibition of bacterial-associated infection and enhancement of in vivo osseointegration, Surf. Coating. Technol. 405 (2021).
[17] E.C. Wisdom, Y. Zhou, C. Chen, C. Tamerler, M.L. Snead, Mitigation of peri-implantitis by rational design of bifunctional peptides with antimicrobial properties, ACS Biomater. Sci. Eng. 6 (2020) 2682–2695.
[18] B. Wang, A. Bian, F. Jia, J. Lan, H. Yang, K. Yan, L. Xie, H. Qiao, X. Chang, H. Lin, H. Zhang, Y. Huang, "Dual-functional" strontium titanate nanotubes designed based on fusion peptides simultaneously enhancing anti-infection and osseointegration, Biomater. Adv. 133 (2022) 112650.
[19] B. Wang, J. Lan, H. Qiao, L. Xie, H. Yang, H. Lin, X. Li, Y. Huang, Porous surface with fusion peptides embedded in strontium titanate nanotubes elevates osteogenic and antibacterial activity of additively manufactured titanium alloy, Colloids Surf. B Biointerfaces 224 (2023) 113188.
[20] M. Hoyos-Nogues, F. Velasco, M.P. Ginebra, J.M. Manero, F.J. Gil, C. Mas-Moruno, Regenerating bone via multifunctional coatings: the blending of cell integration and bacterial inhibition properties on the surface of biomaterials, ACS Appl. Mater. Interfaces 9 (2017) 21618–21630.
[21] W. Zhang, C. Ling, H. Liu, A. Zhang, L. Mao, J. Wang, J. Chao, L.J. Backman, Q. Yao, J. Chen, Tannic acid-mediated dual peptide-functionalized scaffolds to direct stem cell behavior and osteochondral regeneration, Chem. Eng. J. 396 (2020).
[22] H. Zhao, Y. Huang, W. Zhang, Q. Guo, W. Cui, Z. Sun, D. Eglin, L. Liu, G. Pan, Q. Shi, Mussel-Inspired peptide coatings on titanium implant to improve osseointegration in osteoporotic condition, ACS Biomater. Sci. Eng. 4 (2018) 2505–2515.
[23] J. Sun, Y. Huang, H. Zhao, J. Niu, X. Ling, C. Zhu, L. Wang, H. Yang, Z. Yang, G. Pan, Q. Shi, Bio-clickable mussel-inspired peptides improve titanium-based material osseointegration synergistically with immunopolarization-regulation, Bioact. Mater. 9 (2022) 1–14.
[24] M. Wang, Y. Deng, P. Zhou, Z. Luo, Q. Li, B. Xie, X. Zhang, T. Chen, D. Pei, Z. Tang, S. Wei, In vitro culture and directed osteogenic differentiation of human pluripotent stem cells on peptides-decorated two-dimensional microenvironment, ACS Appl. Mater. Interfaces 7 (2015) 4560–4572.
[25] L.D. Campora, C. Metzger, S. Dahnhardt-Pfeiffer, R. Drexel, F. Meier, S. Furtauer, Fluorescence labeling of cellulose nanocrystals-A facile and green synthesis route, Polymers 14 (2022).
[26] N. Khan, H. Mukhtar, Tea polyphenols in promotion of human health, Nutrients 11 (2018).
[27] E. Torre, Molecular signaling mechanisms behind polyphenol-induced bone anabolism, Phytochemistry Rev. 16 (2017) 1183–1226.
[28] E. Koren, R. Kohen, H. Ovadia, I. Ginsburg, Bacteria coated by polyphenols acquire potent oxidant-scavenging capacities, Exp. Biol. Med. 234 (2009) 940–951.
[29] B. Zhao, Y. Dong, X. Shen, W. He, H. Jin, Y. Lili, S.W. Zheng, X. Zan, J. Liu, Construction of multifunctional coating with cationic amino acid-coupled peptides for osseointegration of implants, Mater Today Bio 23 (2023) 100848.
[30] V. Gribova, R. Auzely-Velty, C. Picart, Polyelectrolyte multilayer assemblies on materials surfaces: from cell adhesion to tissue engineering, Chem. Mater. 24 (2012) 854–869.
[31] K.M. Meek, J.B. Weiss, Differential fixation of poly(L-arginine) and poly(L-lysine) by tannic acid and its application to the fixation of collagen in electron microscopy, Biochim. Biophys. Acta 587 (1979) 112–120.
[32] S.J. Lee, J.E. Won, C. Han, X.Y. Yin, H.K. Kim, H. Nah, I.K. Kwon, B.H. Min, C. H. Kim, Y.S. Shin, S.A. Park, Development of a three-dimensionally printed scaffold grafted with bone forming peptide-1 for enhanced bone regeneration with in vitro and in vivo evaluations, J. Colloid Interface Sci. 539 (2019) 468–480.
[33] N. Cini, F. Calisir, Layer-by-layer self-assembled emerging systems for nanosized drug delivery, Nanomedicine (Lond) 17 (2022) 1961–1980.
[34] S. Yang, Y. Wang, X. Wu, S. Sheng, T. Wang, X. Zan, Multifunctional tannic acid (TA) and lysozyme (Lys) films built layer by layer for potential application on implant coating, ACS Biomater. Sci. Eng. 5 (2019) 3582–3594.
[35] N.C. Speller, N. Siraj, B.P. Regmi, H. Marzoughi, C. Neal, I.M. Warner, Rational design of QCM-D virtual sensor arrays based on film thickness, viscoelasticity, and harmonics for vapor discrimination, Anal. Chem. 87 (2015) 5156–5166.
[36] K. Nakajima, M. Ito, D. Wang, H. Liu, H.K. Nguyen, X. Liang, A. Kumagai, S. Fujinami, Nano-palpation AFM and its quantitative mechanical property mapping, Microscopy (Oxf) 63 (2014) 193–208.
[37] M.E. Dokukin, I. Sokolov, Quantitative mapping of the elastic modulus of soft materials with HarmoniX and PeakForce QNM AFM modes, Langmuir 28 (2012) 16060–16071.
[38] S. Yang, Y. Wang, S. Luo, C. Shan, Y. Geng, T. Zhang, S. Sheng, X. Zan, Building polyphenol and gelatin films as implant coating, evaluating from in vitro and in vivo performances, Colloids Surf. B Biointerfaces 181 (2019) 549–560.
[39] R. Lu, B. Zhao, L. Yang, S. Zheng, X. Zan, N. Li, Role of driving force on engineering layer-by-layer protein/polyphenol coating with flexible structures and properties, ACS Appl. Mater. Interfaces 15 (2023) 20551–20562.
[40] R. Lu, X. Zhang, X. Cheng, X. Zan, W. Geng, Secondary structure-dominated layer-by-layer growth mode of protein coatings, Langmuir 37 (2021) 13000–13011.
[41] X. Zan, P. Sitasuwan, S. Feng, Q. Wang, Effect of roughness on in situ biomineralized CaP-collagen coating on the osteogenesis of mesenchymal stem cells, Langmuir 32 (2016) 1808–1817.
[42] A. Schneider, G. Francius, R. Obeid, P. Schwinté, J. Hemmerlé, B. Frisch, P. Schaaf, J.C. Voegel, B. Senger, C. Picart, Polyelectrolyte multilayers with a tunable Young's modulus: influence of film stiffness on cell adhesion, Langmuir 22 (2006) 1193–1200.
[43] L. Richert, A.J. Engler, D.E. Discher, C. Picart, Elasticity of native and cross-linked polyelectrolyte multilayer films, Biomacromolecules 5 (2004) 1908–1916.
[44] B. Schoeler, N. Delorme, I. Doench, G.B. Sukhorukov, A. Fery, K. Glinel, Polyelectrolyte films based on polysaccharides of different conformations: effects on multilayer structure and mechanical properties, Biomacromolecules 7 (2006) 2065–2071.
[45] S. Jin, R. Yang, C. Hu, S. Xiao, Y. Zuo, Y. Man, Y. Li, J. Li, Plant-derived polyphenol and LL-37 peptide-modified nanofibrous scaffolds for promotion of antibacterial activity, anti-inflammation, and type-H vascularized bone regeneration, ACS Appl. Mater. Interfaces 15 (2023) 7804–7820.
[46] A.G. Gristina, Biomaterial-centered infection: microbial adhesion versus tissue integration, Science 237 (1987) 1588–1595.
[47] X.Z. Shu, K. Ghosh, Y. Liu, F.S. Palumbo, Y. Luo, R.A. Clark, G.D. Prestwich, Attachment and spreading of fibroblasts on an RGD peptide-modified injectable hyaluronan hydrogel, J. Biomed. Mater. Res. 68 (2004) 365–375.
[48] X. Trepat, Z. Chen, K. Jacobson, Cell migration, Compr. Physiol. 2 (2012) 2369–2392.
[49] Y. Song, C. Zhang, P. Wang, L. Wang, C. Bao, M.D. Weir, M.A. Reynolds, K. Ren, L. Zhao, H.H.K. Xu, Engineering bone regeneration with novel cell-laden hydrogel microfiber-injectable calcium phosphate scaffold, Mater. Sci. Eng., C 75 (2017) 895–905.
[50] J. Pijuan, C. Barcelo, D.F. Moreno, O. Maiques, P. Siso, R.M. Marti, A. Macia, A. Panosa, In vitro cell migration, invasion, and adhesion assays: from cell imaging to data analysis, Front. Cell Dev. Biol. 7 (2019) 107.
[51] H. Sies, D.P. Jones, Reactive oxygen species (ROS) as pleiotropic physiological signalling agents, Nat. Rev. Mol. Cell Biol. 21 (2020) 363–383.
[52] K. Brieger, S. Schiavone, F.J. Miller Jr., K.H. Krause, Reactive oxygen species: from health to disease, Swiss Med. Wkly. 142 (2012) w13659.
[53] P. Zhou, X. Hou, Y. Chao, W. Yang, W. Zhang, Z. Mu, J. Lai, F. Lv, K. Yang, Y. Liu, J. Li, J. Ma, J. Luo, S. Guo, Synergetic interaction between neighboring platinum and ruthenium monomers boosts CO oxidation, Chem. Sci. 10 (2019) 5898–5905.
[54] X. Zhang, Z. Li, P. Yang, G. Duan, X. Liu, Z. Gu, Y. Li, Polyphenol scaffolds in tissue engineering, Mater. Horiz. 8 (2021) 145–167.
[55] S. Vimalraj, Alkaline phosphatase: structure, expression and its function in bone mineralization, Gene 754 (2020) 144855.
[56] J. Shu, A. Tan, Y. Li, H. Huang, J. Yang, The correlation between serum total alkaline phosphatase and bone mineral density in young adults, BMC Muscoskel. Disord. 23 (2022) 467.
[57] A. Bernar, J.V. Gebetsberger, M. Bauer, W. Streif, M. Schirmer, Optimization of the alizarin red S assay by enhancing mineralization of osteoblasts, Int. J. Mol. Sci. 24 (2022).
[58] M. Saito, K. Marumo, Effects of collagen crosslinking on bone material properties in health and disease, Calcif. Tissue Int. 97 (2015) 242–261.
[59] C. Shan, A. Ghosh, X.Z. Guo, S.M. Wang, Y.F. Hou, S.T. Li, J.M. Liu, Roles for osteocalcin in brain signalling: implications in cognition- and motor-related disorders, Mol. Brain 12 (2019) 23.
[60] T. Komori, Regulation of osteoblast differentiation by Runx2, Adv. Exp. Med. Biol. 658 (2010) 43–49.
[61] Z. Bin-Bin, Z.X. Da-Wa, L. Chao, Z. Lan-Tao, W. Tao, L. Chuan, L. Chao-Zheng, L. De-Chun, F. Chang, W. Shu-Qing, D. Zu-Nan, P. Xian-Wei, Z.X. Zhang, L. Ke-Wen, M2 macrophagy-derived exosomal miRNA-26a-5p induces osteogenic differentiation of bone mesenchymal stem cells, J. Orthop. Surg. Res. 17 (2022) 137.
[62] G. Wang, Y. Zhu, X. Zan, M. Li, Endowing orthopedic implants' antibacterial, antioxidation, and osteogenesis properties through a composite coating of nano-hydroxyapatite, tannic acid, and lysozyme, Front. Bioeng. Biotechnol. 9 (2021) 718255.
[63] Y. Zhu, D. Zhou, X. Zan, Q. Ye, S. Sheng, Engineering the surfaces of orthopedic implants with osteogenesis and antioxidants to enhance bone formation in vitro and in vivo, Colloids Surf. B Biointerfaces 212 (2022) 112319.
[64] E. Shevroja, F.P. Cafarelli, G. Guglielmi, D. Hans, DXA parameters, Trabecular Bone Score (TBS) and Bone Mineral Density (BMD), in fracture risk prediction in endocrine-mediated secondary osteoporosis, Endocrine 74 (2021) 20–28.
[65] D.J. Lin, C.P. Ju, S.H. Huang, Y.C. Tien, H.S. Yin, W.C. Chen, J.H. Chern Lin, Mechanical testing and osteointegration of titanium implant with calcium phosphate bone cement and autograft alternatives, J. Mech. Behav. Biomed. Mater. 4 (2011) 1186–1195.
[66] X. Yang, Q. Wang, C. Yan, D. Huang, Y. Zhang, H. He, S. Xiong, C. Li, P. Chen, T. Ye, D. Hu, L. Wang, A dual-functional strontium-decorated titanium implants that guides the immune response for osseointegration of osteoporotic rats, Colloids Surf. B Biointerfaces 233 (2024) 113643.
[67] T. Du, J. Liu, J. Dong, H. Xie, X. Wang, X. Yang, Y. Yang, Multifunctional coatings of nickel-titanium implant toward promote osseointegration after operation of bone tumor and clinical application: a review, Front. Bioeng. Biotechnol. 12 (2024) 1325707.
[68] S. Zhao, X. Zhou, J. Dang, Y. Wang, J. Jiang, T. Zhao, D. Sun, C. Chen, X. Dai, Y. Liu, M. Zhang, Construction of a layer-by-layer self-assembled rosemarinic acid

delivery system on the surface of CFRPEEK implants for enhanced anti-inflammatory and osseointegration activities, J. Mater. Chem. B 12 (2024) 3031–3046.